1 **Structural and functional analysis of a potent sarbecovirus neutralizing antibody**

2

3 Dora Pinto[1,7], Young-Jun Park[2,7], Martina Beltramello[1,7], Alexandra C. Walls[2,7], M.

4 Alejandra Tortorici[2,3], Siro Bianchi[1], Stefano Jaconi[1], Katja Culap[1], Fabrizia Zatta[1],

5 Anna De Marco[1], Alessia Peter[1], Barbara Guarino[1], Roberto Spreafico[4], Elisabetta

6 Cameroni[1], James Brett Case[6], Rita E. Chen[6], Colin Havenar-Daughton[4], Gyorgy

7 Snell[4], Amalio Telenti[4], Herbert W. Virgin[4], Antonio Lanzavecchia[1,5], Michael S.

8 Diamond[6], Katja Fink[1], David Veesler[2*] and Davide Corti[1*]

9

10 [1] Humabs Biomed SA, a subsidiary of Vir Biotechnology, 6500 Bellinzona, Switzerland.
11 [2] Department of Biochemistry, University of Washington, Seattle, Washington 98195, USA.
12 [3] Institut Pasteur & CNRS UMR 3569, Unité de Virologie Structurale, 75015, Paris, France.
13 [4] Vir Biotechnology, San Francisco, California 94158, USA
14 [5] Institute for Research in Biomedicine, Università della Svizzera Italiana, 6500 Bellinzona,
15 Switzerland.
16 [6] Departments of Medicine, Molecular Microbiology, Pathology & Immunology, Washington
17 University School of Medicine, St. Louis, MO 631110, USA
18 [7] These authors contributed equally
19

20 Correspondence: dveesler@uw.edu, dcorti@vir.bio

21

22

23 **SARS-CoV-2 is a newly emerged coronavirus responsible for the current COVID-**
24 **19 pandemic that has resulted in more than one million infections and 73,000**
25 **deaths[1,2]. Vaccine and therapeutic discovery efforts are paramount to curb the**
26 **pandemic spread of this zoonotic virus. The SARS-CoV-2 spike (S) glycoprotein**
27 **promotes entry into host cells and is the main target of neutralizing antibodies.**
28 **Here we describe multiple monoclonal antibodies targeting SARS-CoV-2 S**
29 **identified from memory B cells of a SARS survivor infected in 2003. One**
30 **antibody, named S309, potently neutralizes SARS-CoV-2 and SARS-CoV**
31 **pseudoviruses as well as authentic SARS-CoV-2 by engaging the S receptor-**
32 **binding domain. Using cryo-electron microscopy and binding assays, we show**
33 **that S309 recognizes a glycan-containing epitope that is conserved within the**
34 **sarbecovirus subgenus, without competing with receptor attachment. Antibody**
35 **cocktails including S309 along with other antibodies identified here further**
36 **enhanced SARS-CoV-2 neutralization and may limit the emergence of**
37 **neutralization-escape mutants. These results pave the way for using S309 and**
38 **S309-containing antibody cocktails for prophylaxis in individuals at high risk of**
39 **exposure or as a post-exposure therapy to limit or treat severe disease.**

40

41   Coronavirus entry into host cells is mediated by the transmembrane spike (S)
42 glycoprotein that forms homotrimers protruding from the viral surface[3]. The S
43 glycoprotein comprises two functional subunits: S_1 (divided into A, B, C and D domains)
44 that is responsible for binding to host cell receptors and S_2 that promotes fusion of the
45 viral and cellular membranes[4,5]. Both SARS-CoV-2 and SARS-CoV belong to the
46 sarbecovirus subgenus and their S glycoproteins share 80% amino acid sequence
47 identity[6]. SARS-CoV-2 S is closely related to the bat SARS-related CoV (SARSr-CoV)
48 RaTG13 with which it shares 97.2% amino acid sequence identity[1]. We and others
49 recently demonstrated that human angiotensin converting enzyme 2 (hACE2) is a
50 functional receptor for SARS-CoV-2, as is the case for SARS-CoV[1,6-8]. The S domain
51 B (S^B) is the receptor binding domain (RBD) and binds to hACE2 with high-affinity,
52 possibly contributing to the current rapid SARS-CoV-2 transmission in humans[6,9], as
53 previously proposed for SARS-CoV[10].

54   As the coronavirus S glycoprotein mediates entry into host cells, it is the main
55 target of neutralizing antibodies and the focus of therapeutic and vaccine design
56 efforts[3]. The S trimers are extensively decorated with N-linked glycans that are
57 important for protein folding[11] and modulate accessibility to host proteases and
58 neutralizing antibodies[12-15]. Cryo-electron microscopy (cryoEM) structures of SARS-
59 CoV-2 S in two distinct functional states[6,9] along with cryoEM and crystal structures of
60 SARS-CoV-2 S^B in complex with hACE2[16-18] revealed dynamic states of S^B domains,
61 providing a blueprint for the design of vaccines and inhibitors of viral entry.

62   Passive administration of monoclonal antibodies (mAbs) could have a major
63 impact on controlling the SARS-CoV-2 pandemic by providing immediate protection,
64 complementing the development of prophylactic vaccines. Accelerated development
65 of mAbs in a pandemic setting could be reduced to 5-6 months compared to the
66 traditional timeline of 10-12 months (Kelley B., Developing monoclonal antibodies at
67 pandemic speed, Nat Biotechnol, in press). The recent finding that ansuvimab
68 (mAb114) is a safe and effective treatment for symptomatic Ebola virus infection is a
69 striking example of the successful use of mAb therapy during an infectious disease
70 outbreak[19,20]. We previously isolated potently neutralizing human mAbs from memory
71 B cells of individuals infected with SARS-CoV[21] or MERS-CoV[22]. Passive transfer of
72 these mAbs protected animals challenged with various SARS-CoV isolates and SARS-
73 related CoV (SARSr-CoV)[21,23,24], as well as with MERS-CoV[22]. Structural
74 characterization of two of these mAbs in complex with SARS-CoV S and MERS-CoV

75   S provided molecular-level information on the mechanisms of viral neutralization[14]. In

76   particular, while both mAbs blocked S^B attachment to the host receptor, the SARS-

77   CoV-neutralizing S230 mAb acted by functionally mimicking receptor-attachment and

78   promoting S fusogenic conformational rearrangements[14]. Another mechanism of

79   SARS-CoV neutralization was recently described for mAb CR3022, which bound a

80   cryptic epitope only accessible when at least two out of the three S^B domains of a S

81   trimer were in the open conformation[25,26]. However, none of these mAbs neutralize

82   SARS-CoV-2.

83

84   **Identification of a potent SARS-CoV-2 neutralizing mAb from a SARS survivor**

85   We previously identified a set of human neutralizing mAbs from an individual

86   infected with SARS-CoV in 2003 that potently inhibited both human and zoonotic

87   SARS-CoV isolates[21,23,27]. To characterize the potential cross-reactivity of these

88   antibodies with SARS-CoV-2, we performed a new memory B cell screening using

89   peripheral blood mononuclear cells collected in 2013 from the same patient. We

90   describe here nineteen mAbs from the initial screen (2004 blood draw)[21,23] and six

91   mAbs from the new screen (2013 blood draw). The identified mAbs had a broad V

92   gene usage and were not clonally related (**Table 1).** Eight out of the twenty five mAbs

93   bound to SARS-CoV-2 S and SARS-CoV S transfected CHO cells with EC_{50} values

94   ranging between 1.4 and 6,100 ng/ml, and 0.8 and 254 ng/ml, respectively **(Fig. 1a-**

95   **b)**. MAbs were further evaluated for binding to the SARS-CoV-2 and SARS-CoV S^B

96   domains as well as to the prefusion-stabilized OC43 S[28], MERS-CoV S[29,30], SARS-

97   CoV S[30] and SARS-CoV-2 S[6] ectodomain trimers. None of the mAbs studied bound to

98   prefusion OC43 S or MERS-CoV S ectodomain trimers, indicating a lack of cross-

99   reactivity outside the sarbecovirus subgenus **(Extended Data Fig.1)**. MAbs S303,

100   S304, S309 and S315 recognized the SARS-CoV-2 and SARS-CoV RBDs. In

101   particular, S309 bound with nanomolar affinity to both S^B domains, as determined by

102   biolayer interferometry **(Fig. 1c-d, Extended Data Fig. 2)**. Unexpectedly, S306 and

103   S310 stained cells expressing SARS-CoV-2 S at higher levels than those expressing

104   SARS-CoV S, yet it did not interact with SARS-CoV-2 or SARS-CoV S ectodomain

105   trimers and RBD constructs by ELISA. These results suggest that they may recognize

106   post-fusion SARS-CoV-2 S, which was recently proposed to be abundant on the

107   surface of authentic SARS-CoV-2 viruses[31] **(Fig. 1a-b and Extended Data Fig.3)**.

108　　　　To evaluate the neutralization potency of the SARS-CoV-2 cross-reactive
109　　mAbs, we carried out pseudovirus neutralization assays using a murine leukemia virus
110　　(MLV) pseudotyping system[32]. S309 showed comparable neutralization potencies
111　　against both SARS-CoV and SARS-CoV-2 pseudoviruses, whereas S303 neutralized
112　　SARS-CoV-MLV but not SARS-CoV-2-MLV. S304 and S315 weakly neutralized
113　　SARS-CoV-MLV and SARS-CoV-2-MLV (**Extended Data Fig.4**). In addition, S309
114　　neutralized SARS-CoV-MLVs from isolates of the 3 phases of the 2002-2003 epidemic
115　　with IC_{50} values comprised between 120 and 180 ng/ml and partially neutralized the
116　　SARSr-CoV[33] WIV-1 (**Fig. 1e**). Finally, mAb S309 potently neutralized authentic
117　　SARS-CoV-2 (2019n-CoV/USA_WA1/2020) with an IC_{50} of 69 ng/ml (**Fig. 1f**).

118

119　　**Structural basis of S309 cross-neutralization of SARS-CoV-2 and SARS-CoV**

120　　　　　To study the mechanisms of S309-mediated neutralization, we characterized
121　　the complex between the S309 Fab fragment and a prefusion stabilized SARS-CoV-2
122　　S ectodomain trimer[6] using single-particle cryoEM. Similar to our previous study of apo
123　　SARS-CoV-2 S[6], 3D classification of the cryoEM data enabled identification of two
124　　structural states: a trimer with one S^B domain open and a closed trimer. We determined
125　　3D reconstructions of the SARS-CoV-2 S ectodomain trimer with a single open S^B
126　　domain and in a closed state (applying 3-fold symmetry), both with three S309 Fabs
127　　bound, at 3.7 Å and 3.3 Å resolution, respectively (**Fig. 2a-c, Extended Data Fig. 5**
128　　**and Table 2)**. In parallel, we also determined a crystal structure of the S309 Fab at 3.3
129　　Å resolution to assist model building (**Table 3**). The S309 Fab bound to the open S^B
130　　domain is weakly resolved in the cryoEM map, due to marked conformational variability
131　　of the upward pointing S^B domain, and was not modeled in density. The analysis below
132　　is based on the closed state structure.

133　　　　　S309 recognizes a protein/glycan epitope on the SARS-CoV-2 S^B, distinct from
134　　the receptor-binding motif. The epitope is accessible in both the open and closed S
135　　states, explaining the stoichiometric binding of Fab to the S trimer (**Fig. 2a-c**). The
136　　S309 paratope is composed of all six CDR loops that burie a surface area of ~1,050Å^2
137　　at the interface with S^B through electrostatic interactions and hydrophobic contacts.
138　　The 20-residue long CDRH3 sits atop the S^B helix comprising residues 337-344 and
139　　also contacts the edge of the S^B five-stranded β-sheet (residues 356-361), overall
140　　accounting for ~50% of the buried surface area (**Fig. 2d-e**). CDRL1 and CDRL2 extend
141　　the epitope by interacting with the helix spanning residues 440-444 that is located near

4

142   the S 3-fold molecular axis. CDRH3 and CDRL2 sandwich the SARS-CoV-2 S glycan

143   at position N343 through contacts with the core fucose moiety (in agreement with the

144   detection of SARS-CoV-2 N343 core-fucosylated peptides by mass-spectrometry[34])

145   and to a lesser extent with the core N-acetyl-glucosamine (Fig. 2d). These latter

146   interactions bury an average surface of ~170 Å^2 and stabilize the N343 oligosaccharide

147   which is resolved to a much larger extent than in the apo SARS-CoV-2 S structures[6,9].

148   The structural data explain the S309 cross-reactivity between SARS-CoV-2 and

149   SARS-CoV as 19 out of 24 residues of the epitope are strictly conserved (**Fig. 2f** and

150   **Extended Data Fig. 6a-b)**. $R346_{SARS-CoV-2}$, $R357_{SARS-CoV-2}$, $N354_{SARS-CoV-2}$ and

151    $L441_{SARS-CoV-2}$ are conservatively substituted to $K333_{SARS-CoV}$, $K344_{SARS-CoV}$ (except for

152   SARS-CoV isolate GZ02 where it is $R444_{SARS-CoV}$), $E341_{SARS-CoV}$ and $I428_{SARS-CoV}$

153   whereas $K444_{SARS-CoV-2}$ is semi-conservatively substituted to $T431_{SARS-CoV}$, in

154   agreement with the comparable binding affinities to SARS-CoV and SARS-CoV-2 S

155   (**Fig. 1c).** The oligosaccharide at position N343 is also conserved in both viruses and

156   corresponds to SARS-CoV N330, for which we previously detected core-fucosylated

157   glycopeptides by mass spectrometry[14] which would allow for similar interactions with

158   the S309 Fab. Analysis of the S glycoprotein sequences of the 2,229 SARS-CoV-2

159   isolates reported to date indicates that several mutations have occurred with variable

160   frequency on the SARS-CoV-2 S ectodomain (**Extended Data Fig. 7a-b**) but no

161   mutations arose within the epitope recognized by S309 mAb. Finally, S309 contact

162   residues showed a high degree of conservation across clade 1, 2 and 3 sarbecovirus

163   human and animal isolates[35] (**Extended Data Fig. 7c).** Collectively, the structural data

164   indicate that S309 could neutralize all SARS-CoV-2 isolates circulating to date and

165   possibly most other zoonotic sarbecoviruses.

166

167   **Mechanism of S309-mediated neutralization of SARS-CoV-2 and SARS-CoV**

168   The cryoEM structure of S309 bound to SARS-CoV-2 S presented here

169   combined with the structures of SARS-CoV-2 S^B and SARS-CoV S^B in complex with

170   ACE2[16-18,36] indicate that the Fab engages an epitope distinct from the receptor-binding

171   motif and would not clash with ACE2 upon binding to S **(Figure 3a-b)**. Biolayer

172   interferometry analysis of S309 Fab or IgG binding to the SARS-CoV-2 S^B domain or

173   the S ectodomain trimer confirmed the absence of competition between the mAb and

174   ACE2 for binding to SARS-CoV-2 S **(Figure 3c and Extended Data Fig. 8)**.

175   To further investigate the mechanism of S309-mediated neutralization, we

176   compared side-by-side transduction of SARS-CoV-2-MLV in the presence of either

177   S309 Fab or S309 IgG. Both experiments yielded comparable IC_{50} values (3.8 and 3.5

178   nM, respectively), indicating similar potencies for IgG and Fab **(Fig. 3d)**. However, The

179   S309 IgG reached 100% neutralization, whereas the S309 Fab plateaued at ~80%

180   neutralization **(Fig. 3d)**. This result indicates that one or more IgG-specific bivalent

181   mechanisms, such as S trimer cross-linking, steric hindrance or aggregation of

182   virions[37], may contribute to the ability to fully neutralize pseudovirions.

183   Fc-dependent effector mechanisms, such as NK-mediated antibody-dependent

184   cell cytotoxicity (ADCC) and antibody-dependent cellular phagocytosis (ADCP) can

185   contribute to viral control in infected individuals. We observed efficient S309- and

186   S306-mediated ADCC of SARS-CoV-2 S-transfected cells, whereas the other mAbs

187   tested showed limited or no activity (**Fig. 3e and Extended Data Fig. 9a**). These

188   findings might be related to distinct binding orientations and/or positioning of the mAb

189   Fc fragment relative to the FcγRIIIa receptors. ADCC was observed only using NK

190   (effector) cells expressing the high-affinity FcγRIIIa variant (V158) but not the low-

191   affinity variant (F158) (**Fig. 3e**). These results, which we confirmed using a FcγRIIIa

192   cell reporter assay (**Fig. 3f**), suggest that S309 Fc engineering could potentially

193   enhance activation of NK cells with the low-affinity FcγRIIIa variant (F158)[38].

194   Macrophage or dendritic cell-mediated ADCP can contribute to viral control by clearing

195   virus and infected cells and by stimulating T cell response via presentation of viral

196   antigens[39,40]. Similar to the ADCC results, mAbs S309 and S306 showed the strongest

197   ADCP response (**Fig. 3g** and **Extended Data Fig. 8b)**. FcγRIIa signaling, however,

198   was only observed for S309 (**Fig. 3h**). These findings suggest that ADCP by

199   monocytes was dependent on both FcγRIIIa and FcγRIIa engagement. Collectively,

200   these results demonstrate that in addition to potent *in vitro* neutralization, S309 may

201   leverage additional protective mechanisms *in vivo*, as previously shown for other

202   antiviral antibodies[41,42].

203

MAb cocktails enhance SARS-CoV-2 neutralization

205   To gain more insight into the epitopes recognized by our panel of mAbs, we

206   used   structural   information,   escape   mutants   analysis   [23,27,30],   and   biolayer

207   inteferometry-based epitope binning to map the antigenic sites present on the SARS-

208 CoV and SARS-CoV-2 S^B domains (**Fig. 4a and Extended Data Fig.10**). This analysis

209 identified at least four antigenic sites within the S^B domain of SARS-CoV targeted by

210 our panel of mAbs. The receptor-binding motif, which is targeted by S230, S227 and

211 S110, is termed site I. Sites II and III are defined by S315 and S124, respectively, and

212 the two sites were bridged by mAb S304. Site IV is defined by S309, S109, and S303

213 mAbs. Given the lower number of mAbs cross-reacting with SARS-CoV-2, we were

214 able to identify sites IV targeted by S309 and S303, and site II-III targeted by S304 and

215 S315 (**Fig. 4b**).

216   Based on the above findings, we evaluated the neutralization potency of the site

217 IV S309 mAb in combination with either the site II S315 mAb or site II-III S304 mAb.

218 Although S304 and S315 alone were weakly neutralizing, the combination of either of

219 these mAbs with S309 resulted in an enhanced neutralization potency, compared to

220 single mAbs, against both SARS-CoV-2-MLV and authentic SARS-CoV-2 **(Fig. 4c-d**

221 and **Fig. 1e)**. A synergistic effect between two non-competing anti-RBD mAbs has

222 been already reported for SARS-CoV[43] and our data extend this observation to SARS-

223 CoV-2, providing a proof-of-concept for the use of mAbs combinations to prevent or

224 control SARS-CoV-2.

225   In summary, our study identifies S309 as a human mAb with broad neutralizing

226 activity against multiple sarbecoviruses, including SARS-CoV-2, via recognition of a

227 highly conserved epitope in the S^B domain comprising the N343-glycan (N330 in

228 SARS-CoV S). Furthermore, S309 can recruit effector mechanisms and synergizes

229 with weakly neutralizing mAbs, which may mitigate the risk of viral escape. Our data

230 indicate the potential to discover potently neutralizing pan-sarbecovirus mAbs,

231 highlight antigenic sites to include in vaccine design, and pave the way to support

232 preparedness for future sarbecovirus outbreaks. As S309 bears the promise to be an

233 effective countermeasure to curtail the COVID-19 pandemic caused by SARS-CoV-2,

234 Fc variants of S309 with increased half-life and effector functions have entered an

235 accelerated development path towards clinical trials.

236

237

238

239

ACKNOWLEDGEMENTS

AUTHOR CONTRIBUTIONS

A.C.W., K.F., M.S.D., D.V. and D.C. designed the experiments. A.C.W., M.A.T., S.J., E.C. expressed and purified the proteins. K.C., F.Z., S.J., E.C. sequenced and expressed antibodies. D.P., M.B., A.C.W. and S.B. performed binding assays. D.P., M.B., A.C.W., A.P., A.D.M. carried out pseudovirus neutralization assays. J.B.C., R.E.C. performed neutralization assays with authentic SARS-CoV-2. B.G. performed effector function assays. Y.J.P. prepared samples for cryoEM and collected the data. Y.J.P. and D.V. processed the data, built and refined the atomic models. A.C.W. crystallized the S309 Fab. Y.J.P. collected and processed the X-ray diffraction data and built and refined the atomic model. R.S., A.T. and G.S. performed bioinformatic and conservation analysis. A.L. provided key reagents. A.C.W., K.F., C.H.D., H.W.V., A.L., D.V., D.C. analyzed the data and prepared the manuscript with input from all authors.

DECLARATION OF INTERESTS

D.P., S.B., K.C., E.C., C.H-D., G.S., M.B., A.K., K.F., A.P. F.Z., S.J., B.G., A.D.M., A.L., A.T., H.W.V, R.S. and D.C. are employees of Vir Biotechnology Inc. and may hold shares in Vir Biotechnology Inc. M.S.D. is a consultant for Inbios, Eli Lilly, Vir Biotechnology, NGM Biopharmaceuticals, and Emergent BioSolutions and on the Scientific Advisory Board of Moderna. The Diamond laboratory at Washington

273 University School of Medicine has received sponsored research agreements from

274 Moderna. The other authors declare no competing financial interests.

275

276

277 **MATERIALS AND METHODS**

278

279 **Ethics statement**

280 Donors provided written informed consent for the use of blood and blood components

281 (such as sera), following approval by the Canton Ticino Ethics Committee, Switzerland.

282

283 **Antibody discovery and expression**

284 Monoclonal antibodies were isolated from EBV-immortalized memory B cells.

285 Recombinant antibodies were expressed in ExpiCHO cells transiently co-transfected

286 with plasmids expressing the heavy and light chain, as previously described[44]. Abs

287 S303, S304, S306, S309, S310 and S315 were expressed as rIgG-LS antibodies. The

288 LS mutation confers a longer half-life in vivo[45]. Antibodies S110 and S124 tested in

289 Fig. 1 and Extended Data Fig. 1 were purified mAbs produced from immortalized B

290 cells.

291

292 **Transient expression of recombinant SARS-CoV-2 protein and flow cytometry**

293 The full-length S gene of SARS-CoV-2 strain (SARS-CoV-2-S) isolate

294 BetaCoV/Wuhan-Hu-1/2019 (accession number MN908947) was codon optimized for

295 human cell expression and cloned into the phCMV1 expression vector (Genlantis).

296 Expi-CHO cells were transiently transfected with phCMV1-SARS-CoV-2-S, SARS-

297 spike_pcDNA.3 (strain SARS) or empty phCMV1 (Mock) using Expifectamine

298 CHO Enhancer. Two days after transfection, cells were collected for immunostaining

299 with mAbs. An Alexa647-labelled secondary antibody anti-human IgG Fc was used for

300 detection. Binding of mAbs to transfected cells was analyzed by flow-cytometry using a

301 ZE5 Cell Analyzer (Biorard) and FlowJo software (TreeStar). Positive binding was

302 defined by differential staining of CoV-S-transfectants versus mock-transfectants.

303

304 **Affinity determination and competition experiments using Octet (BLI, biolayer**

305 **interferometry)**

306 KD determination of full-length antibodies: Protein A biosensors (Pall ForteBio) were

307 used to immobilize recombinant antibodies at 2.7 μg/ml for 1min, after a hydration step

308 for 10 min with Kinetics Buffer (KB; 0.01% endotoxin-free BSA, 0.002% Tween-20,

309 0.005% NaN3 in PBS). Association curves were recorded for 5 minutes by incubating

310 the mAb-coated sensors with different concentration of SARS-CoV RBD (Sino

311 Biological) or SARS-CoV-2 RBD (produced in house; residues 331-550 of spike protein

312 from BetaCoV/Wuhan-Hu-1/2019, accession number MN908947). The highest RBD

313 concentration was 10 μg/ml, then serially diluted 1:2.5. Dissociation was recorded for

314 9 minutes by moving the sensors to wells containing KB. KD values were calculated

315 using a global fit model (Octet). Octet Red96 (ForteBio) equipment was used.

316 KD determination of full-length antibodies compared to Fab: His-tagged RBD of SARS-

317 CoV or SARS-CoV-2 were loaded at 3 μg/ml in KB for 15 minutes onto anti-HIS (HIS2)

318 biosensors (Molecular Devices, ForteBio). Association of mAb and Fab was performed

319 in KB at 15 μg/ml and 5 μg/ml respectively for 5 minutes. Dissociation in KB was

320 measured for 10 minutes.

321   MAbs competition experiments: His-tagged RBD of SARS-CoV or SARS-CoV-

322 2 was loaded for 5 minutes at 3 μg/ml in KB onto anti-Penta-HIS (HIS1K) biosensors

323 (Molecular Devices, ForteBio). Association of mAbs was performed in KB at 15 μg/ml.

324   ACE2 competition experiments: ACE2-His (Bio-Techne AG) was loaded for 30

325 minutes at 5 μg/ml in KB onto anti-HIS (HIS2) biosensors (Molecular Devices-

326 ForteBio).

327 SARS-CoV RBD-rabbitFc or SARS-CoV-2 RBD-mouseFc (Sino Biological Europe

328 GmbH) at 1 μg/ml was associated for 15 minutes, after a preincubation with or without

329 Ab (30 μg/ml, 30 minutes). Dissociation was monitored for 5 minutes.

330

331 **ELISA**

332 The following proteins were coated on 96 well ELISA plates at the following

333 concentrations: SARS-CoV RBD (Sino Biological, 40150-V08B1) at 1 μg/ml, SARS-

334 CoV-2 RBD (produced in house) at 10 μg/ml, ectodomains (stabilized prefusion trimer)

335 of SARS-CoV, SARS-CoV-2, OC43 and MERS, all at 1ug/ml. After blocking with 1%

336 BSA in PBS, antibodies es were added to the plates in a concentration range between

337 5 and 0.000028 μg/ml and incubated for 1 h at RT. Plates were washed and secondary

338 Ab Goat Anti Human IgG-AP (Southern Biotechnology: 2040-04) was added.

10

339 Substrate P-NitroPhenyl Phosphate (pNPP) (Sigma-Aldrich 71768) was used for

340 colour development. OD405 was read on an ELx808IU plate reader (Biotek).

341

342 **Measurement of Fc-effector functions**

343 ADCC assays were performed using ExpiCHO-S cells transient transfected with

344 SARS-CoV or SARS-CoV-2 S as targets. Target cells were incubated with titrated

345 concentrations of mAbs and after 10 minutes incubated with primary human NK cells

346 as effector cells at an effector:target ratio of 9:1. NK cells were isolated from fresh

347 blood of healthy donors using the MACSxpress NK Isolation Kit (Miltenyi Biotec, Cat.

348 Nr.: 130-098-185). ADCC was measured using LDH release assay (Cytotoxicity

349 Detection Kit (LDH) (Roche; Cat. Nr.: 11644793001) after 4 hours of incubation at

350 37°C.

351 ADCP assays were performed using ExpiCHO-S target cells transiently transfected

352 with SARS-CoV-2 S and fluorescently labeled with PKH67 Fluorescent Cell Linker Kits

353 (Sigma Aldrich, Cat. Nr.: MINI67) as targets. Target cells were incubated with titrated

354 concentrations of mAbs for 10minutes, followed by incubation with human PBMCs

355 isolated from healthy donors that were fluorescently labeled with Cell Trace Violet

356 (Invitrogen, Cat. Nr.: C34557) at an effector:target ratio of 20:1. After an overnight

357 incubation at 37°C, cells were stained with anti-human CD14-APC antibody (BD

358 Pharmingen, Cat. Nr.: 561708, Clone M5E2) to stain monocytes. Antibody-mediated

359 phagocytosis was determined by flow cytometry, gating on CD14$^+$ cells that were

360 double positive for cell trace violet and PKH67.

361 Determination of mAb-dependent activation of human FcγRIIIa or FcγRIIa was

362 performed using ExpiCHO cells transiently transfected with SARS-CoV-2 S

363 (BetaCoV/Wuhan-Hu-1/2019), incubated with titrated concentrations of mAbs for 10

364 minutes. ExpiCHO cells then were incubated with Jurkat cells expressing FcγRIIIa

365 receptor or FcγRIIa on their surface and stably transfected with NFAT-driven luciferase

366 gene (Promega, Cat. Nr.: G9798 and G7018) at an effector to target ratio of 6:1 for

367 FcγRIIIa and 5:1 for FcγRIIa. Activation of human FcγRs in this bioassay results in the

368 NFAT-mediated expression of the luciferase reporter gene. Luminescence was

369 measured after 21 hours of incubation at 37°C with 5% CO_2, using the Bio-Glo-TM

370 Luciferase Assay Reagent according to the manufacturer's instructions.

371

11

Pseudovirus neutralization assays

Murine leukemia virus (MLV)-based SARS-CoV S-pseudotyped viruses were prepared as previously described[6,32]. HEK293T cells were co-transfected with a SARS-CoV, SARS-CoV-2, CUHK, GZ02, or WiV1 S encoding-plasmid, an MLV Gag-Pol packaging construct and the MLV transfer vector encoding aluciferase reporter using the Lipofectamine 2000 transfection reagent (Life Technologies) according to the manufacturer's instructions. Cells were incubated for 5 hours at 37°C with 8% CO_2 with OPTIMEM transfection medium. DMEM containing 10% FBS was added for 72 hours. VeroE6 cells or DBT cells transfected with human ACE2 were cultured in DMEM containing 10% FBS, 1% PenStrep and plated into 96 well plates for 16-24 hours. Concentrated pseudovirus with or without serial dilution of antibodies was incubated for 1 hour and then added to the wells after washing 3X with DMEM. After 2-3 hours DMEM containing 20% FBS and 2% PenStrep was added to the cells for 48 hours. Following 48 hours of infection, One-Glo-EX (Promega) was added to the cells and incubated in the dark for 5-10 minutes prior to reading on a Varioskan LUX plate reader (ThermoFisher). Measurements were done in duplicate and relative luciferase units (RLU) were converted to percent neutralization and plotted with a non-linear regression curve fit in PRISM.

Live virus neutralization assay

SARS-CoV-2 strain 2019-nCoV/USA_WA1/2020 was obtained from the Centers for Disease Control and Prevention (gift of Natalie Thornburg). Virus was passaged once in Vero CCL81 cells (ATCC) and titrated by focus-forming assay on Vero E6 cells. Serial dilutions of indicated mAbs were incubated with 10^2 focus forming units (FFU) of SARS-CoV-2 for 1 hour at 37°C. MAb-virus complexes were added to Vero E6 cell monolayers in 96-well plates and incubated at 37°C for 1 hour. Subsequently, cells were overlaid with 1% (w/v) methylcellulose in MEM supplemented with 2% FBS. Plates were harvested 30 hours later by removing overlays and fixed with 4% PFA in PBS for 20 minutes at room temperature. Plates were washed and sequentially incubated with 1 μg/mL of CR3022[46] anti-S antibody and HRP-conjugated goat anti-human IgG in PBS supplemented with 0.1% saponin and 0.1% BSA. SARS-CoV-2-infected cell foci were visualized using TrueBlue peroxidase substrate (KPL) and

404   quantitated on an ImmunoSpot microanalyzer (Cellular Technologies). Data were

405   processed using Prism software (GraphPad Prism 8.0).

406

Recombinant Spike ectodomain production

408   The SARS-CoV-2 2P S (Genbank: YP_009724390.1) ectodomain was produced in

409   500mL cultures of HEK293F cells grown in suspension using FreeStyle 293 expression

410   medium (Life technologies) at 37°C in a humidified 8% CO2 incubator rotating at 130

411   r.p.m, as previously reported[6]. The culture was transfected using 293fectin

412   (ThermoFisher Scientific) with cells grown to a density of 10^6 cells per mL and

413   cultivated for three days. The supernatant was harvested and cells were resuspended

414   for another three days, yielding two harvests. Clarified supernatants were purified

415   using a 5mL Cobalt affinity column (Takara). Purified protein was filtered or

416   concentrated and flash frozen in a buffer containing 50 mM Tris pH 8.0 and 150 mM

417   NaCl prior to cryoEM analysis. The SARS-CoV S, HCoV-OC43 S and MERS-CoV S

418   constructs were previously described[14,28] and produced similarly to SARS-CoV-2 2P

419   S.

420

CryoEM sample preparation and data collection.

422   3 µL of SARS-CoV-2 S at 1.6 mg/mL was mixed with 0.45 µL of S309 Fab at 7.4 mg/mL

423   for 1 min at room temperature before application onto a freshly glow discharged 1.2/1.3

424   UltraFoil grid (300 mesh). Plunge freezing used a vitrobot MarkIV (ThermoFisher

425   Scientific) using a blot force of 0 and 6.5 second blot time at 100% humidity and 25°C.

426   Data were acquired using the Leginon software [47] to control an FEI Titan Krios

427   transmission electron microscope operated at 300 kV and equipped with a Gatan K2

428   Summit direct detector and Gatan Quantum GIF energy filter, operated in zero-loss

429   mode with a slit width of 20 eV. Automated data collection was carried out using

430   Leginon at a nominal magnification of 130,000x with a pixel size of 0.525 Å with tilt

431   angles ranging between 20˚ and 50˚, as previously described[48]. The dose rate was

432   adjusted to 8 counts/pixel/s, and each movie was acquired in super-resolution mode

433   fractionated in 50 frames of 200 ms. 3,900 micrographs were collected in a single

434   session with a defocus range comprised between 1.0 and 3.0 µm.

435

436

437

CryoEM data processing

Movie frame alignment, estimation of the microscope contrast-transfer function parameters, particle picking and extraction were carried out using Warp [49]. Particle images were extracted with a box size of 800 binned to 400 yielding a pixel size of 1.05 Å. For each data set two rounds of reference-free 2D classification were performed using cryoSPARC [50] to select well-defined particle images. Subsequently, two rounds of 3D classification with 50 iterations each (angular sampling 7.5° for 25 iterations and 1.8° with local search for 25 iterations), using our previously reported closed SARS-CoV-2 S structure[6] as initial model, were carried out using Relion [51] without imposing symmetry to separate distinct SARS-CoV-2 S conformations. 3D refinements were carried out using non-uniform refinement along with per-particle defocus refinement in cryoSPARC[50]. Particle images were subjected to Bayesian polishing [52] before performing another round of non-uniform refinement in cryoSPARC [50] followed by per-particle defocus refinement and again non-uniform refinement. Reported resolutions are based on the gold-standard Fourier shell correlation (FSC) of 0.143 criterion and Fourier shell correlation curves were corrected for the effects of soft masking by high-resolution noise substitution[53].

CryoEM model building and analysis.

UCSF Chimera [54] and Coot were used to fit atomic models (PDB 6VXX and PDB 6VYB) into the cryoEM maps. The Fab was subsequently manually built using Coot[55,56]. N-linked glycans were hand-built into the density where visible and the models were refined and relaxed using Rosetta[57]. Glycan refinement relied on a dedicated Rosetta protocol, which uses physically realistic geometries based on prior knowledge of saccharide chemical properties [58], and was aided by using both sharpened and unsharpened maps. Models were analyzed using MolProbity [59], EMringer [60], Phenix [61] and privateer [62] to validate the stereochemistry of both the protein and glycan components. Figures were generated using UCSF ChimeraX [63].

Crystallization and X-ray structure determination of Fab S309

Fab S309 crystals were grown in hanging drop set up with a mosquito at 20°C using 150 nL protein solution in Tris HCl pH 8.0, 150 mM NaCl and 150nL mother liquor solution containing 1.1 M Sodium Malonate, 0.1 M HEPES, pH 7.0 and 0.5% (w/v) Jeffamine ED-2001. Crystals were cryo-protected using the mother liquor solution

472 supplemented with 30% glycerol. The dataset was collected at ALS beamline 5.0.2

473 and processed to 3.3 Å resolution in space group $P4_12_12$ using mosflm[64] and

474 Aimless[65]. The structure of Fab S309 was solved by molecular replacement using

475 Phaser[66] and homology models as search models. The coordinates were improved

476 and completed using Coot[55] and refined with REFMAC5[67]. Crystallographic data

477 collection and refinement statistics are shown in Table 3.

478

479 **Sequence alignment**

480 SARS-CoV-2 genomics sequences were downloaded from GISAID on March

481 29th 2020, using the "complete (>29,000 bp)" and "low coverage exclusion" filters. Bat

482 and pangolin sequences were removed to yield human-only sequences. The spike

483 ORF was localized by performing reference protein (YP_009724390.1)-genome

484 alignments with GeneWise2. Incomplete matches and indel-containing ORFs were

485 rescued and included in downstream analysis. Nucleotide sequences were

486 translated *in silico* using seqkit. Sequences with more than 10% undetermined

487 aminoacids (due to N basecalls) were removed. Multiple sequence alignment was

488 performed using MAFFT. Variants were determined by comparison of aligned

489 sequences (n=2,229) to the reference sequence using the R/Bioconductor package

490 Biostrings. A similar strategy was used to extract and translate spike protein

491 sequences from SARS-CoV genomes sourced from ViPR (search criteria: SARS-

492 related coronavirus, full-length genomes, human host, deposited before December

493 2019 to exclude SARS-CoV-2, n=53). Sourced SARS-CoV genome sequences

494 comprised all the major published strains, such as Urbani, Tor2, TW1, P2, Frankfurt1,

495 among others. Pangolin sequences as shown by Tsan-Yuk Lam et al[68] were sourced

496 from GISAID. Bat sequences from the three clades of sarbecoviruses as shown by Lu

497 et al[35] were sourced from Genbank. Civet and racoon dog sequences were similarly

498 sourced from Genbank.

499

500

15

501
502 **References**

503 1   Zhou, P. *et al.* A pneumonia outbreak associated with a new coronavirus of
504   probable bat origin. *Nature*, doi:10.1038/s41586-020-2012-7 (2020).
505 2   Zhu, N. *et al.* A Novel Coronavirus from Patients with Pneumonia in China,
506   2019. *N Engl J Med*, doi:10.1056/NEJMoa2001017 (2020).
507 3   Tortorici, M. A. & Veesler, D. Structural insights into coronavirus entry. *Adv Virus*
508   *Res* **105**, 93-116, doi:10.1016/bs.aivir.2019.08.002 (2019).
509 4   Walls, A. C. *et al.* Cryo-electron microscopy structure of a coronavirus spike
510   glycoprotein trimer. *Nature* **531**, 114-117, doi:10.1038/nature16988
511 10.1038/nature16988. Epub 2016 Feb 8. (2016).
512 5   Walls, A. C. *et al.* Tectonic conformational changes of a coronavirus spike
513   glycoprotein promote membrane fusion. *Proceedings of the National Academy*
514   *of Sciences* **114**, 11157-11162, doi:10.1073/pnas.1708727114 (2017).
515 6   Walls, A. C. *et al.* Structure, function and antigenicity of the SARS-CoV-2 spike
516   glycoprotein.   *bioRxiv*,   2020.2002.2019.956581,
517   doi:10.1101/2020.02.19.956581 (2020).
518 7   Hoffmann, M. *et al.* SARS-CoV-2 Cell Entry Depends on ACE2 and TMPRSS2
519   and Is Blocked by a Clinically Proven Protease Inhibitor. *Cell*,
520   doi:10.1016/j.cell.2020.02.052 (2020).
521 8   Letko, M., Marzi, A. & Munster, V. Functional assessment of cell entry and
522   receptor usage for SARS-CoV-2 and other lineage B betacoronaviruses. *Nature*
523   *Microbiology*, doi:10.1038/s41564-020-0688-y (2020).
524 9   Wrapp, D. *et al.* Cryo-EM structure of the 2019-nCoV spike in the prefusion
525   conformation. *Science*, doi:10.1126/science.abb2507 (2020).
526 10   Li, W. *et al.* Receptor and viral determinants of SARS-coronavirus adaptation to
527   human ACE2. *EMBO J* **24**, 1634-1643, doi:10.1038/sj.emboj.7600640
528 10.1038/sj.emboj.7600640. Epub 2005 Mar 24. (2005).
529 11   Rossen, J. W. *et al.* The viral spike protein is not involved in the polarized sorting
530   of coronaviruses in epithelial cells. *J Virol* **72**, 497-503 (1998).
531 12   Walls, A. C. *et al.* Glycan shield and epitope masking of a coronavirus spike
532   protein observed by cryo-electron microscopy. *Nat Struct Mol Biol* **23**, 899-905,
533   doi:10.1038/nsmb.3293
534 10.1038/nsmb.3293. Epub 2016 Sep 12. (2016).
535 13   Xiong, X. *et al.* Glycan shield and fusion activation of a deltacoronavirus spike
536   glycoprotein fine-tuned for enteric infections. *J Virol*, doi:10.1128/JVI.01628-17
537 10.1128/JVI.01628-17. (2017).
538 14   Walls, A. C. *et al.* Unexpected Receptor Functional Mimicry Elucidates
539   Activation of Coronavirus Fusion. *Cell* **176**, 1026-1039 e1015,
540   doi:10.1016/j.cell.2018.12.028
541 10.1016/j.cell.2018.12.028. Epub 2019 Jan 31. (2019).
542 15   Yang, Y. *et al.* Two Mutations Were Critical for Bat-to-Human Transmission of
543   Middle East Respiratory Syndrome Coronavirus. *J Virol* **89**, 9119-9123,
544   doi:10.1128/JVI.01279-15
545 10.1128/JVI.01279-15. Epub 2015 Jun 10. (2015).
546 16   Yan, R. *et al.* Structural basis for the recognition of SARS-CoV-2 by full-length
547   human ACE2. *Science* **367**, 1444-1448, doi:10.1126/science.abb2762 (2020).
548 17   Shang, J. *et al.* Structural basis of receptor recognition by SARS-CoV-2. *Nature*,
549   doi:10.1038/s41586-020-2179-y (2020).

550   18   Lan, J. *et al.* Structure of the SARS-CoV-2 spike receptor-binding domain bound
551   to the ACE2 receptor. *Nature*, doi:10.1038/s41586-020-2180-5 (2020).
552   19   Corti, D. *et al.* Protective monotherapy against lethal Ebola virus infection by a
553   potently neutralizing antibody. *Science* **351**, 1339-1342,
554   doi:10.1126/science.aad5224 (2016).
555   20   Levine, M. M. Monoclonal Antibody Therapy for Ebola Virus Disease. *N Engl J*
556   *Med* **381**, 2365-2366, doi:10.1056/NEJMe1915350 (2019).
557   21   Traggiai, E. *et al.* An efficient method to make human monoclonal antibodies
558   from memory B cells: potent neutralization of SARS coronavirus. *Nat Med* **10**,
559   871-875, doi:10.1038/nm1080
560   10.1038/nm1080. Epub 2004 Jul 11. (2004).
561   22   Corti, D. *et al.* Prophylactic and postexposure efficacy of a potent human
562   monoclonal antibody against MERS coronavirus. *Proc Natl Acad Sci U S A* **112**,
563   10473-10478, doi:10.1073/pnas.1510199112
564   10.1073/pnas.1510199112. Epub 2015 Jul 27. (2015).
565   23   Rockx, B. *et al.* Structural basis for potent cross-neutralizing human monoclonal
566   antibody protection against lethal human and zoonotic severe acute respiratory
567   syndrome coronavirus challenge. *J Virol* **82**, 3220-3235,
568   doi:10.1128/JVI.02377-07
569   10.1128/JVI.02377-07. Epub 2008 Jan 16. (2008).
570   24   Menachery, V. D. *et al.* SARS-like WIV1-CoV poised for human emergence.
571   *Proc Natl Acad Sci U S A* **113**, 3048-3053, doi:10.1073/pnas.1517719113
572   10.1073/pnas.1517719113. Epub 2016 Mar 14. (2016).
573   25   Yuan, M. *et al.* A highly conserved cryptic epitope in the receptor-binding
574   domains of SARS-CoV-2 and SARS-CoV. *Science*,
575   doi:10.1126/science.abb7269 (2020).
576   26   Joyce, M. G. *et al.* A Cryptic Site of Vulnerability on the Receptor Binding
577   Domain of the SARS-CoV-2 Spike Glycoprotein. *bioRxiv*,
578   2020.2003.2015.992883, doi:10.1101/2020.03.15.992883 (2020).
579   27   Rockx, B. *et al.* Escape from human monoclonal antibody neutralization affects
580   in vitro and in vivo fitness of severe acute respiratory syndrome coronavirus. *J*
581   *Infect Dis* **201**, 946-955, doi:10.1086/651022
582   10.1086/651022. (2010).
583   28   Tortorici, M. A. *et al.* Structural basis for human coronavirus attachment to sialic
584   acid receptors. *Nat Struct Mol Biol* **26**, 481-489, doi:10.1038/s41594-019-0233-
585   y (2019).
586   29   Park, Y. J. *et al.* Structures of MERS-CoV spike glycoprotein in complex with
587   sialoside attachment receptors. *Nat Struct Mol Biol* **26**, 1151-1157,
588   doi:10.1038/s41594-019-0334-7 (2019).
589   30   Walls, A. C. *et al.* Unexpected Receptor Functional Mimicry Elucidates
590   Activation of Coronavirus Fusion. *Cell* **176**, 1026-1039.e1015,
591   doi:10.1016/j.cell.2018.12.028 (2019).
592   31   Liu, C. *et al.* Viral Architecture of SARS-CoV-2 with Post-Fusion Spike Revealed
593   by Cryo-EM. *bioRxiv*, 2020.2003.2002.972927,
594   doi:10.1101/2020.03.02.972927 (2020).
595   32   Millet, J. K. & Whittaker, G. R. Murine Leukemia Virus (MLV)-based Coronavirus
596   Spike-pseudotyped Particle Production and Infection. *Bio Protoc* **6**,
597   doi:10.21769/BioProtoc.2035
598   10.21769/BioProtoc.2035. (2016).

599   33   Ge, X. Y. *et al.* Isolation and characterization of a bat SARS-like coronavirus
600   that uses the ACE2 receptor. *Nature* **503**, 535-538, doi:10.1038/nature12711
601   10.1038/nature12711. Epub 2013 Oct 30. (2013).
602   34   Watanabe, Y., Allen, J. D., Wrapp, D., McLellan, J. S. & Crispin, M. Site-specific
603   analysis of the SARS-CoV-2 glycan shield. *bioRxiv*, 2020.2003.2026.010322,
604   doi:10.1101/2020.03.26.010322 (2020).
605   35   Lu, R. *et al.* Genomic characterisation and epidemiology of 2019 novel
606   coronavirus: implications for virus origins and receptor binding. *Lancet* **395**,
607   565-574, doi:10.1016/S0140-6736(20)30251-8 (2020).
608   36   Li, F., Li, W., Farzan, M. & Harrison, S. C. Structure of SARS coronavirus spike
609   receptor-binding domain complexed with receptor. *Science* **309**, 1864-1868,
610   doi:10.1126/science.1116480 (2005).
611   37   Klasse, P. J. & Sattentau, Q. J. Occupancy and mechanism in antibody-
612   mediated neutralization of animal viruses. *J Gen Virol* **83**, 2091-2108,
613   doi:10.1099/0022-1317-83-9-2091 (2002).
614   38   Wang, X., Mathieu, M. & Brezski, R. J. IgG Fc engineering to modulate antibody
615   effector functions. *Protein Cell* **9**, 63-73, doi:10.1007/s13238-017-0473-8
616   (2018).
617   39   He, W. *et al.* Alveolar macrophages are critical for broadly-reactive antibody-
618   mediated protection against influenza A virus in mice. *Nat Commun* **8**, 846,
619   doi:10.1038/s41467-017-00928-3 (2017).
620   40   DiLillo, D. J. & Ravetch, J. V. Differential Fc-Receptor Engagement Drives an
621   Anti-tumor Vaccinal Effect. *Cell* **161**, 1035-1045, doi:10.1016/j.cell.2015.04.016
622   (2015).
623   41   Corti, D. *et al.* A neutralizing antibody selected from plasma cells that binds to
624   group 1 and group 2 influenza A hemagglutinins. *Science* **333**, 850-856,
625   doi:10.1126/science.1205669 (2011).
626   42   Hessell, A. J. *et al.* Fc receptor but not complement binding is important in
627   antibody protection against HIV. *Nature* **449**, 101-104,
628   doi:10.1038/nature06106 (2007).
629   43   ter Meulen, J. *et al.* Human monoclonal antibody combination against SARS
630   coronavirus: synergy and coverage of escape mutants. *PLoS Med* **3**, e237,
631   doi:10.1371/journal.pmed.0030237 (2006).
632   44   Stettler, K. *et al.* Specificity, cross-reactivity, and function of antibodies elicited
633   by Zika virus infection. *Science* **353**, 823-826, doi:10.1126/science.aaf8505
634   (2016).
635   45   Zalevsky, J. *et al.* Enhanced antibody half-life improves in vivo activity. *Nat
636   Biotechnol* **28**, 157-159, doi:10.1038/nbt.1601 (2010).
637   46   Tian, X. *et al.* Potent binding of 2019 novel coronavirus spike protein by a SARS
638   coronavirus-specific human monoclonal antibody. *Emerg Microbes Infect* **9**,
639   382-385, doi:10.1080/22221751.2020.1729069 (2020).
640   47   Suloway, C. *et al.* Automated molecular microscopy: the new Leginon system.
641   *Journal of structural biology* **151**, 41-60, doi:10.1016/j.jsb.2005.03.010 (2005).
642   48   Tan, Y. Z. *et al.* Addressing preferred specimen orientation in single-particle
643   cryo-EM through tilting. *Nat Methods* **14**, 793-796, doi:10.1038/nmeth.4347
644   (2017).
645   49   Tegunov, D. & Cramer, P. Real-time cryo-electron microscopy data
646   preprocessing with Warp. *Nature methods*, doi:10.1038/s41592-019-0580-y
647   (2019).

648 50 Punjani, A., Rubinstein, J. L., Fleet, D. J. & Brubaker, M. A. cryoSPARC:
649   algorithms for rapid unsupervised cryo-EM structure determination. *Nature*
650   *methods* **14**, 290-296, doi:10.1038/nmeth.4169 (2017).
651 51 Zivanov, J. *et al.* New tools for automated high-resolution cryo-EM structure
652   determination in RELION-3. *Elife* **7**, doi:10.7554/eLife.42166
653 10.7554/eLife.42166. (2018).
654 52 Zivanov, J., Nakane, T. & Scheres, S. H. W. A Bayesian approach to beam-
655   induced motion correction in cryo-EM single-particle analysis. *IUCrJ* **6**,
656   doi:doi:10.1107/S205225251801463X (2019).
657 53 Scheres, S. H. & Chen, S. Prevention of overfitting in cryo-EM structure
658   determination. *Nature methods* **9**, 853-854, doi:10.1038/nmeth.2115 (2012).
659 54 Goddard, T. D., Huang, C. C. & Ferrin, T. E. Visualizing density maps with UCSF
660   Chimera. *Journal of structural biology* **157**, 281-287,
661   doi:10.1016/j.jsb.2006.06.010 (2007).
662 55 Emsley, P., Lohkamp, B., Scott, W. G. & Cowtan, K. Features and development
663   of Coot. *Acta Crystallogr D Biol Crystallogr* **66**, 486-501,
664   doi:10.1107/S0907444910007493 (2010).
665 56 Brown, A. *et al.* Tools for macromolecular model building and refinement into
666   electron cryo-microscopy reconstructions. *Acta Crystallogr D Biol Crystallogr*
667   **71**, 136-153, doi:10.1107/S1399004714021683 (2015).
668 57 Wang, R. Y. *et al.* Automated structure refinement of macromolecular
669   assemblies from cryo-EM maps using Rosetta. *eLife* **5**, doi:10.7554/eLife.17219
670   (2016).
671 58 Frenz, B. D. R., S.; Borst A.J.; Walls, A.C.; Adolf-Bryfogle, J.; Schief, W.R.;
672   Veesler, D.; DiMaio, F. Automatically fixing errors in glycoprotein structures with
673   Rosetta. *Structure* **27**, 1-6, doi:https://doi.org/10.1016/j.str.2018.09.006 (2019).
674 59 Chen, V. B. *et al.* MolProbity: all-atom structure validation for macromolecular
675   crystallography. *Acta Crystallogr D Biol Crystallogr* **66**, 12-21,
676   doi:10.1107/S0907444909042073 (2010).
677 60 Barad, B. A. *et al.* EMRinger: side chain-directed model and map validation for
678   3D cryo-electron microscopy. *Nat Methods* **12**, 943-946,
679   doi:10.1038/nmeth.3541
680 10.1038/nmeth.3541. Epub 2015 Aug 17. (2015).
681 61 Liebschner, D. *et al.* Macromolecular structure determination using X-rays,
682   neutrons and electrons: recent developments in Phenix. *Acta Crystallogr D*
683   *Struct Biol* **75**, 861-877, doi:10.1107/S2059798319011471 (2019).
684 62 Agirre, J. *et al.* Privateer: software for the conformational validation of
685   carbohydrate structures. *Nature structural & molecular biology* **22**, 833-834,
686   doi:10.1038/nsmb.3115 (2015).
687 63 Goddard, T. D. *et al.* UCSF ChimeraX: Meeting modern challenges in
688   visualization and analysis. *Protein Sci* **27**, 14-25, doi:10.1002/pro.3235 (2018).
689 64 Battye, T. G., Kontogiannis, L., Johnson, O., Powell, H. R. & Leslie, A. G.
690   iMOSFLM: a new graphical interface for diffraction-image processing with
691   MOSFLM. *Acta Crystallogr D Biol Crystallogr* **67**, 271-281,
692   doi:10.1107/S0907444910048675 (2011).
693 65 Evans, P. R. & Murshudov, G. N. How good are my data and what is the
694   resolution? *Acta Crystallogr D Biol Crystallogr* **69**, 1204-1214,
695   doi:10.1107/S0907444913000061 (2013).
696 66 McCoy, A. J. *et al.* Phaser crystallographic software. *J Appl Crystallogr* **40**, 658-
697   674, doi:10.1107/S0021889807021206 (2007).

698 67 Murshudov, G. N. *et al.* REFMAC5 for the refinement of macromolecular crystal
699   structures. *Acta Crystallogr D Biol Crystallogr* **67**, 355-367,
700   doi:10.1107/S0907444911001314 (2011).
701 68 Lam, T. T. *et al.* Identifying SARS-CoV-2 related coronaviruses in Malayan
702   pangolins. *Nature*, doi:10.1038/s41586-020-2169-0 (2020).
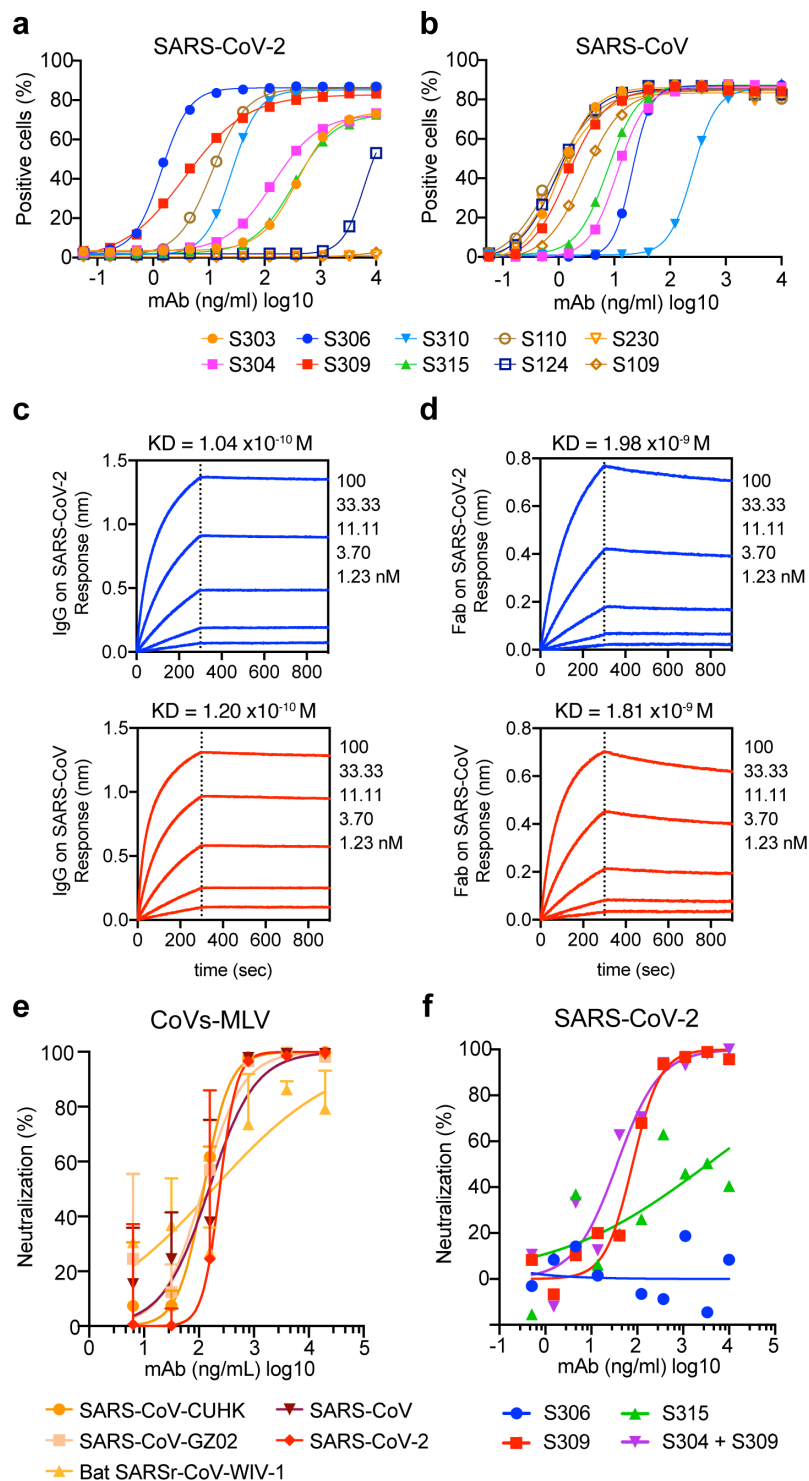703

Figure 1

Figure 1: Identification of a potent SARS-CoV-2 neutralizing mAb from a SARS survivor. a-b, Binding of a panel of mAbs isolated from a SARS-immune patient to the SARS-CoV-2 (**a**) or SARS-CoV (**b**) S glycoproteins expressed at the surface of ExpiCHO cells (symbols are means of duplicates from one experiment). **c-d**, Affinity measurement of S309 full-length IgG1 and Fab for SARS-CoV-2 and SARS-CoV S^B domains measured using biolayer interferometry. **e**, Neutralization of SARS-CoV-2-MLV, SARS-CoV-MLV (bearing S from various isolates) and other sarbecovirus isolates by mAb S309. **f**, Neutralization of authentic SARS-CoV-2 (strain n-CoV/USA_WA1/2020) by mAbs as measured by a focus-forming assay on Vero E6 cells. (**e-f**) mean±SD (**e**) or means (**f**) of duplicates are shown. One representative out of two experiments is shown.
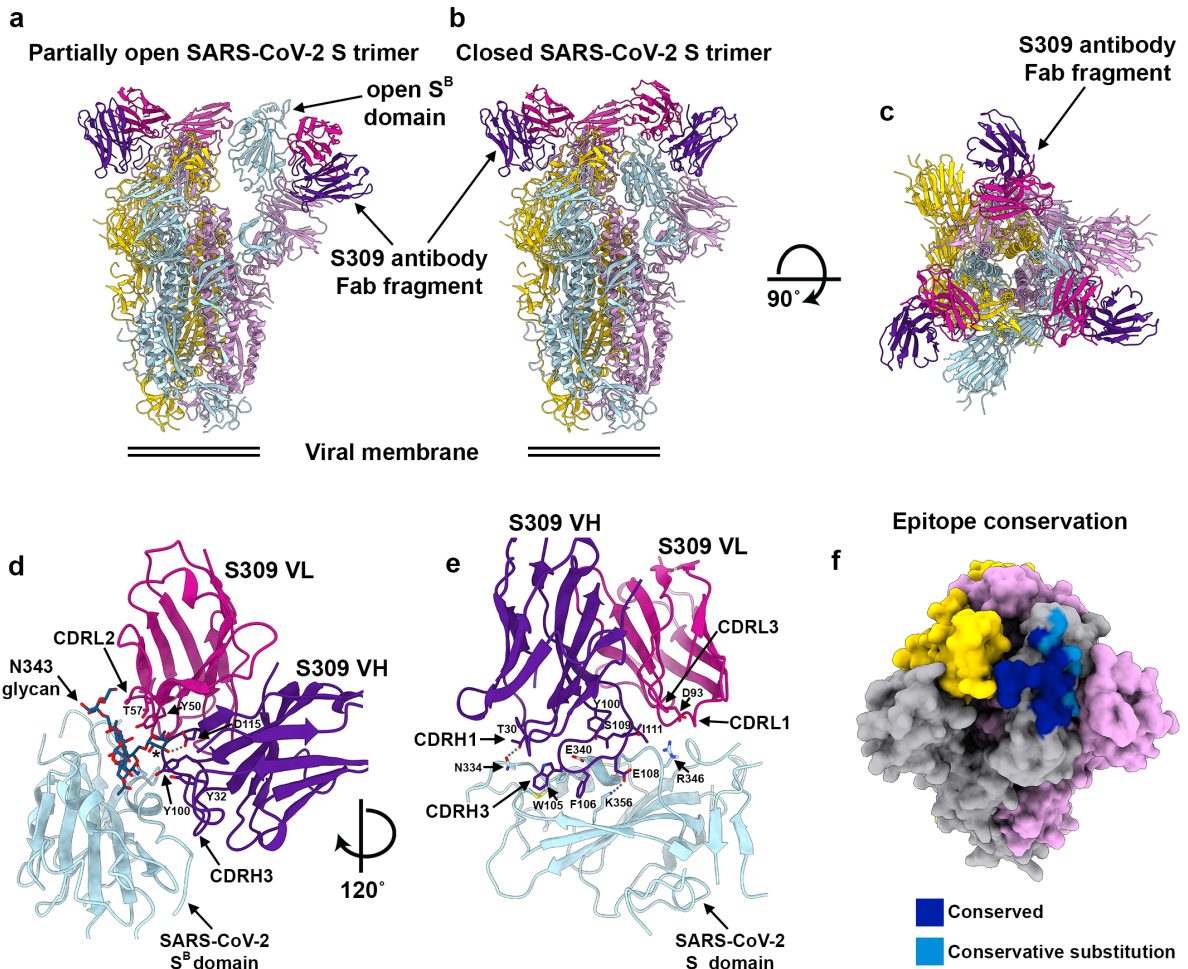
Figure 2

Figure 2: CryoEM structures of the SARS-CoV-2 S glycoprotein in complex with the S309 neutralizing antibody Fab fragment. a, Ribbon diagram of the partially open SARS-CoV-2 S trimer (one S^B domain is open) bound to three S309 Fabs. **b-c,** Ribbon diagrams of the closed SARS-CoV-2 S trimer bound to three S309 Fabs shown in two orthogonal orientations. **d,** Close-up view of the S309 epitope showing the contacts formed with the core fucose (labeled with a star) and the core N-acetyl-glucosamine of the oligosaccharide at position N343. **e,** Close-up view of the S309 epitope showing the 20-residue long CDRH3 siting atop the S^B helix comprising residues 337-344. The oligosaccharide at position N343 is omitted for clarity. In panels (**c-d**), selected residues involved in interactions between S309 and SARS-CoV-2 S are shown. **F,** Molecular surface representation of the SARS-CoV-2 S trimer showing the S309 footprint colored by residue conservation on one protomer among SARS-CoV-2 and SARS-CoV S glycoproteins. The other two protomers are colored pink and gold.
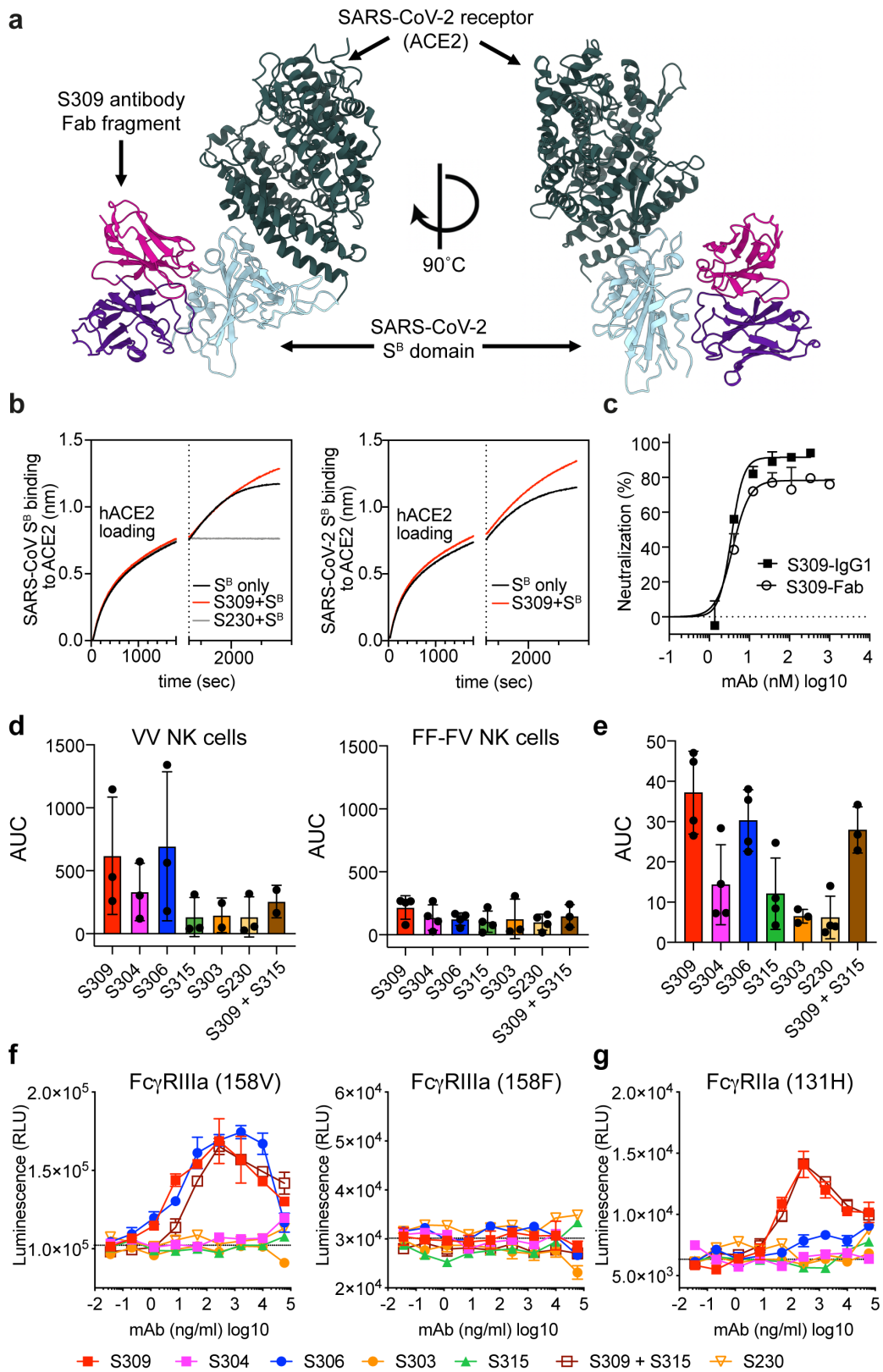
Figure 3

Figure 3: Mechanism of neutralization of S309 mAb. See next page for caption

Figure 3: Mechanism of neutralization of S309 mAb. **a-b**, Ribbon diagrams of S309 and ACE2 bound to SARS-CoV-2 S^B. This composite model was generated using the SARS-CoV-2 S/S309 cryoEM structure reported here and a crystal structure of SARS-CoV-2 S bound to ACE2[16]. **c**, Competition of S309 or S230 mAbs with ACE2 to bind to SARS-CoV S^B (left panel) and SARS-CoV-2 S^B (right panel). ACE2 was immobilized at the surface of biosensors before incubation with S^B domain alone or S^B precomplexed with mAbs. The vertical dashed line indicates the start of the association of mAb-complexed or free S^B to solid-phase ACE2. **d**, Neutralization of SARS-CoV-MLV by S309 IgG1 or S309 Fab, plotted in nM (means $\pm$SD is shown, one out of two experiments is shown). **e**, mAb-mediated ADCC using primary NK effector cells and SARS-CoV-2 S-expressing ExpiCHO as target cells. Bar graph shows the average area under the curve (AUC) for the responses of 3-4 donors genotyped for their FcγRIIIa (mean$\pm$SD, from two independent experiments). **f**, Activation of high affinity (V158) or low affinity (F158) FcγRIIIa was measured using Jurkat reporter cells and SARS-CoV-2 S-expressing ExpiCHO as target cells (one experiment, one or two measurements per mAb). **g**, mAb-mediated ADCP using Cell Trace Violet-labelled PBMCs as phagocytic cells and PKF67-labelled SARS-CoV-2 S-expressing ExpiCHO as target cells. Bar graph shows the average area under the curve (AUC) for the responses of four donor (mean$\pm$SD, from two independent experiments). **h**, Activation of FcγRIIa measured using Jurkat reporter cells and SARS-CoV-2 S-expressing ExpiCHO as target cells (one experiment, one or two measurements per mAb).

Figure 4
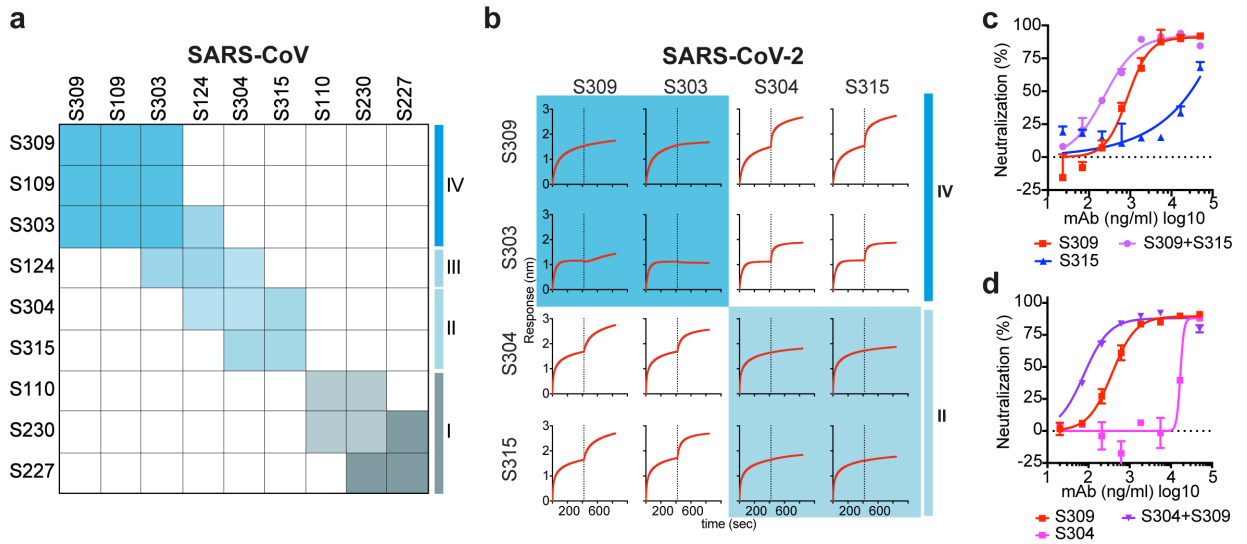
Figure 4: MAb cocktails enhance SARS-CoV-2 neutralization. a, Heat map showing the competition of mAb pairs for binding to the SARS-CoV S^B domain as measured by biolayer interferometry (as shown in Extended Data Fig. 9). **b,** Competition of mAb pairs for binding to the SARS-CoV-2 S^B domain . **c-d,** Neutralization of SARS-CoV-2-MLV by S309 combined with an equimolar amount of S304 or S315 mAbs. For mAb cocktails the concentration on the x axis is that of the individual mAbs.

Table 1: Characteristics of the antibodies described in this study. VH and VL % identity refers to V gene identity compared to germline (IMGT).

mAb	Blood sample date	VH (% identity)	HCDR3 Lenght	HCDR3 sequence	VL (% identity)	LCDR3 sequence	SARS-CoV	SARS-CoV-2	Specificity
S110	2004	VH3-30 (96.88)	18	AKDRFQFARSWYGDYFDY	VK2-30 (96.60)	MQGTHWPPT	+	+	RBD/non-RBD
S124	2004	VH2-26 (98.28)	17	ARINTAAYDYDSTTFDI	VK1-39 (98.57)	QQSYSTPPT	+	+	RBD
S109	2004	VH3-23 (93.75)	19	ARLESATQPLGYYFYGMDV	VL3-25 (97.85)	HSADISATSWV	+	-	RBD
S111	2004	VH3-30 (95.14)	16	ARDIRHLIVVVSDMDV	VK2-30 (98.30)	MQGTHWPPT	+	-	RBD
S127	2004	VH3-30 (96.53)	18	AKDLFGYCRSTSCESLDD	VK1-9 (98.92)	QQLNNYPLT	+	-	RBD
S215	2004	VH3-30 (90.28))	16	ARETRHYSHGLNWFDP	VK3-15 (98.92)	QQYNNWPTT	+	-	RBD
S217	2004	VH3-49 (95.58)	8	SWIHRIVS	VK1-33 (98.21)	QQYDNLPYT	+	-	RBD
S218	2004	VH3-30 (93.40)	16	ARDVKGHIVVMTSLDY	VK2-30 (97.62)	MQGTHWPPT	+	-	RBD
S219	2004	VH1-58(92.01)	18	AAEMATIQNYYYYYGMDV	VK1-39 (95.34)	QQSYSTPPT	+	-	RBD
S222	2006	VH1-2 (91.67)	15	ARGDVPVGTGWVFDF	VK1-39 (92.47)	QQSLSMVT	+	-	RBD
S223	2006	VH3-30 (95.14)	19	ATVSVEGYTSGWYLGTLDF	VK3-15 (98.21)	QQYNNWPGT	+	-	RBD
S224	2006	VH1-18 (90.97)	15	ARQSHSTRGGWHFSP	VK1-39 (95.70)	QQSYSVPYT	+	-	RBD
S225	2006	VH3-9 (96.18)	20	AKDISLVFWSVNPPRNGMDV	VK1-39 (98.57)	QQSYSSPLT	+	-	RBD
S226	2006	VH3-30 (89.61)	18	ARDSSWQSTGWPINWFDR	VK3-11 (96.11)	QQRSNWPPT	+	-	RBD
S227	2006	VH3-23 (95.14)	12	ASPLRNYGDLLY	VK1-5 (96.06)	QQYNSYSWT	+	-	RBD
S228	2006	VH3-30 (96.53)	16	ARDLQMRVVVVSNFDY	VK2D-30 (99.32)	MQATHWPPT	+	-	RBD
S230	2006	VH3-30 (90.97)	20	VTQRDNSRDYFPHYFHDMDV	VK2-30 (97.62)	MQGSHWPPT	+	-	RBD
S231	2006	VH3-30 (90.62)	17	ARDDNLDRHWPLRLGGY	VK2-30 (94.56)	MQGAHWPPT	+	-	RBD
S237	2006	VH3-21 (96.53)	11	ARGFERYYFDS	VL1-44 (96.84)	VAWDDILNAVV	+	-	RBD
S309	2013	VH1-18 (97.22)	20	ARDYTRGAWFGESLIGGFDN	VK3-20 (97.52)	QQHDTSLT	+	+	RBD
S315	2013	VH3-7 (97.92)	17	ARDLWWNDQAHYYGMDV	VL3-25 (97.57)	QSADSSGTV	+	+	RBD
S303	2013	VH3-23 (90.28)	17	ARERDDIFPMGLNAFDI	VK1-5 (97.49)	QQYDTYSWT	+	+	RBD
S304	2013	VH3-13 (97.89)	14	ARGDSSGYYYYFDY	VK1-39 (93.55)	QQSYVSPTYT	+	+	RBD
S306	2013	VH1-18 (95.49)	16	ASDYFDSSGYYHSFDY	VK3-11 (98.92)	QQRSNWPPGCS	+	+	non-RBD
S310	2013	VH1-69 (92.71)	19	ATRTYDSSGYRPYYYGLDV	VL2-23 (97.57)	CSYAGSDTVI	+	+	non-RBD

Table 2. CryoEM data collection and refinement statistics.

	SARS-CoV-2 S + S309 (closed)	SARS-CoV-2 S + S309 (one S^B open)
Data collection and processing		
Magnification	130,000	130,000
Voltage (kV)	300	300
Electron exposure (e⁻/Å²)	70	70
Defocus range (µm)	0.5-3.0	0.5-3.0
Pixel size (Å)	0.525	0.525
Symmetry imposed	C3	C1
Final particle images (no.)	168,449	119,608
Map resolution (Å)	3.3	3.7
FSC threshold	0.143	0.143
Map sharpening B factor (Å²)	-91	-69
Validation		
MolProbity score	0.91	
Clashscore	0.9	
Poor rotamers (%)	0.1	
Ramachandran plot		
Favored (%)	97.24	
Allowed (%)	99.91	
Disallowed (%)	0.09	
EMRinger Score	2.58	

Table 3. X-ray data collection and refinement statistics.

	Fab S309
Data collection	
Space group	$P4_12_12$
Cell constants	
a,b,c (Å)	132.6, 132.6, 301.2
α,β,γ (˚)	90, 90, 90
Wavelength (Å)	0.9812
Resolution (Å)	68.6 - 3.3 (3.48 - 3.30)
Rmerge	18 (75)
$I/\sigma(I)$	13.2 (2)
CC(1/2)	99.0 (33)
Completeness (%)	99.4 (99.0)
Redundancy	12
Refinement	
Resolution (Å)	68.6 - 3.3
Unique reflections	41,395
Rwork/Rfree (%)	20.5 / 23.8
Number of protein atoms	8,347
Number of water atoms	0
R.m.s.d. bond lengths (Å)	0.06
R.m.s.d. bond angles (˚)	1.45
Favored Ramachandran residues (%)	96
Allowed Ramachandran residues (%)	3.54
Disallowed Ramachandran residues (%)	0.46

[1]Numbers in parentheses refer to outer resolution shell